



Cost-effective synthesis of NiO nanoparticles and realization of highly selective NO₂ sensors

Pramod Sharma¹ · Sanjay Kumar² · B. Vishwanadh² · K. G. Girija¹

Received: 11 April 2022 / Accepted: 7 June 2022 / Published online: 1 July 2022
© The Author(s), under exclusive licence to Springer-Verlag GmbH, DE part of Springer Nature 2022

Abstract

Metal oxide nanomaterials approaching grain size less than the Debye length are potential candidates for highly sensitive gas sensors owing to their large surface-to-volume ratio. Hence, research efforts are directed towards cost-effective synthesis of metal oxide nanomaterials for gas-sensor applications. In this context, we report on the facile synthesis and gas sensing studies of NiO nanoparticles (crystallite size ~ 10 nm), prepared by low-cost co-precipitation (NiO_A) and thermochemical (NiO_B) methods. XRD and FESEM confirmed the formation of cubic NiO nanoparticles. UV–Vis spectrometry and photoluminescence studies validated the optical band gap and abundance of defects/vacancies of the NiO nanoparticles. Gas sensors fabricated by spray coating of these nanoparticles on glass substrates revealed high sensitivity, selectivity and reversibility for NO₂ at 180 °C. A plausible sensing mechanism has been suggested based on the interaction of NO₂ with nickel vacancies. Higher sensitivity of co-precipitated nanoparticles has been attributed to the abundance of adsorption sites brought about by the smaller size grains.

Keywords NO₂ gas sensor · Co-precipitation · Thermochemical synthesis · Gas adsorption · Nickel vacancies

1 Introduction

In the modern era, gas sensors have emerged as vital components for safeguarding our environment, home and work place. Accordingly, gas sensors find extensive use in environmental monitoring, medical diagnosis and for regulating various industrial and chemicals processes. Among the perilous gases, NO₂ is one of the major air pollutants, which is considered to be detrimental for our eco-system and human health. Even at a very low concentration of 0.1 ppm, it can cause breathing problems especially in those with asthmatic conditions. Considering the highly reactive and acidic nature of NO₂, over the years the short term exposure limit for NO₂ has been lowered from 5 to 1 ppm by Occupational Safety and Health Administration (OSHA). In recent years, there is a surge in effort for developing simple, selective, sensitive, broad range, cheap and reliable gas sensors with

fast response, pertaining to various applications. As a result, varieties of low-cost gas sensors have been developed and are available commercially such as electrochemical sensors, pellistors and conductometric metal oxide (MOX) sensors [1]. Among these, MOX sensors are the most extensively investigated, owing to their ease of synthesis, low cost, plethora of materials available for gas detection over a wide range and their compatibility with semiconductor processing. Besides, interest in metal oxide nanomaterials is mainly ascribed to their unique inherent properties arising from higher surface-to-volume ratio, dynamic gas-adsorption/diffusion capability, higher surface energy that aids surface reactions, ease of use and reproducible response characteristics [2]. Generally, MOX nanomaterials are classified as n-type or p-type, based on the majority charge carriers, i.e. electrons or holes, respectively. A large number of MOX nanomaterials, namely TiO₂, WO₃, ZnO, SnO₂, CuO and NiO, have been extensively investigated for their gas sensing characteristics [3–6]. From the power consumption point of view, it is generally preferred that the sensor exists in high-impedance state in clean air. When the sensor is exposed to the target gas, the surface conductance of the sensor should increase in proportion to the concentration of the target gas and revert back to the high impedance state when the

✉ K. G. Girija
kgirija@barc.gov.in

¹ Chemistry Division, Bhabha Atomic Research Centre, Mumbai 400085, India

² Materials Science Division, Bhabha Atomic Research Centre, Mumbai 400085, India

sensor is exposed to clean air. Therefore, n-type MOX such as ZnO and SnO₂ are typically used for sensing reducing gases like NH₃, H₂S, CO, where the conductance increases subsequently upon gas exposure [7–9]. Though some of the n-type MOX offer good sensitivity for a host of oxidizing gases, often the change in conductance is beyond the measurable range of simple electronics for commercialization and in addition, they suffer from high power consumption under idle state. Accordingly, p-type MOX such as Cr₂O₃, CuO and NiO are preferred for sensing oxidizing gases. However, research efforts on p-type MOX are limited as they are considered to be inferior compared to n-type MOX. It has been reported that sensitivity of p-type MOX sensor is roughly equal to the square root of that of an n-type MOX sensor for similar synthesis and experimental conditions [10]. Nevertheless, it is well known that the gas sensor performance can be greatly improved by tailoring the size, morphology and doping of the MOX materials using suitable synthesis conditions. In addition, the advent in MOX nanomaterials research has enabled considerable attention towards p-type MOX sensors. Among the widely used p-type MOX, nickel oxide (NiO) has gained a lot of attention due to its distinctive electronic nanostructure, wide band gap (3.6–4.0 eV), remarkable thermal and mechanical stability, low-cost synthesis and environmental compatibility. Thus, NiO has emerged as a promising material for a wide array of applications including catalysis, cathode material for batteries, electrochromic films, magnetic materials and gas sensors [4, 11]. It has been reported that NiO gas sensors are not affected greatly by humidity and the catalytic property of Ni can aid the heterogeneous catalysis reduction of NO_x species, thereby improving the selectivity [12].

As mentioned earlier, the gas sensor response is closely related to nanoparticle size and morphology, which determine the active surface area and gas-diffusion rate, thus affecting the sensor response and selectivity. Since these structural properties of nanoparticles (size, morphology and distribution) depend on synthesis techniques, several methods for synthesizing NiO nanoparticles have been investigated namely, magnetron sputtering, hydrothermal, co-precipitation, sol gel, pulsed laser deposition and micro-emulsion methods [4, 13, 14]. Although a variety of novel morphologies of nanomaterials (nanosheets, nanowire, nanorod, etc.) may give good sensing response, they may not be feasible for large-scale production due to their cost, lack of reproducibility and complexity of synthesis [15]. In this paper, we report on the synthesis of NiO nanoparticles having particle size in range of ~ 10 nm, using two different methods, i.e. widely used co-precipitation [16] and less commonly used thermochemical method [17, 18], utilizing cheap and readily available precursors. The advantages offered by these methods are simple solution phase chemistry and better control on process conditions, which directly influences

the size, morphology and purity of the nanoparticles, thus making these methods attractive for their industrial and technological applications. Further, these nanoparticles were thoroughly investigated for their structural, morphological and NO₂ sensing properties.

2 Experimental

2.1 Synthesis of NiO nanoparticles

NiO nanoparticles were synthesized using anhydrous nickel chloride (NiCl₂), ethylenediamine tetra acetic acid (EDTA), sodium hydroxide (NaOH) and ammonia solution (NH₃) as starting materials.

For the synthesis of NiO nanoparticles by co-precipitation method (NiO_A), 1 M solution of anhydrous NiCl₂ (50 ml), 0.1 M solution of EDTA (25 ml) and 4 M solution of NaOH (20 ml) were prepared. Subsequently, the solution of NiCl₂ and EDTA were mixed together. Here, EDTA was used as a capping agent. The resultant clear solution was stirred at room temperature for ~ 30 min. Afterwards, under constant stirring NaOH solution was added dropwise to the mixture until the pH of the solution reached ~ 12, resulting in formation of greenish precipitate. This green solution was heated at 70 °C for 2 h, under constant stirring. The resultant green precipitate, corresponding to Ni(OH)₂ formation, was washed several times with distilled water for removing reaction residues, until pH ~ 7 was achieved. The obtained green precipitate was dried overnight in the oven at 90 °C.

In thermochemical method (NiO_B), 3 g of anhydrous NiCl₂ was taken in glass beaker and placed in an ice-bath. Subsequently, ~ 30 ml ammonia solution was added slowly (due to exothermic nature of the reaction) over a time-period of ~ 45 min, with intermittent stirring. Eventually a bright bluish coloured clear solution was obtained, resulting in the formation of nickel ammonia complex. Afterwards, under constant stirring at room-temperature distilled water was added to the solution, resulting in formation of green precipitate, which was washed several times until pH of ~ 7 was achieved and later dried overnight at 90 °C.

The green precipitates obtained from both the methods were powdered by grinding and later heated at 350 °C for 3 h in a tubular furnace to obtain of black NiO nanoparticles in powder form. The schematic diagram of the synthesis methods is shown in Fig. S1.

2.2 Characterization of NiO nanoparticles

X-ray diffraction (XRD) analysis of the NiO nanoparticles was accomplished using a Philips powder X-ray diffractometer (Model PW 1071) with Ni filtered Cu-K α radiation (1.5418 Å). Field emission scanning electron microscope

(FESEM) (Carl Zeiss, Model: Auriga 4553) was employed for morphology studies, while energy-dispersive X-ray spectroscopy (EDX) studies were simultaneously carried out using an additional attachment of FESEM (Oxford, Model: X-Max). Transmittance/absorption characteristics were recorded by UV–visible spectrophotometer (JASCO V-650), and room-temperature photoluminescence spectra were studied by fluorescence spectrometer (FLSP 920, Edinburgh Instruments).

2.3 Gas sensing studies

For the gas sensing studies, measured quantities of NiO nanoparticles were dispersed in methanol and sonicated for ~30 min. The supernatant was used to prepare thin films of NiO nanoparticles by spray coating at room temperature on glass substrates using syringe pump (Holmarc model no. HO-TH-04BT). The films were dried at 50 °C for two hours on a hot plate. Gas sensors were fabricated

by thermal evaporation of gold interdigitated electrodes on the thin films. Gas sensing studies were performed in a custom built static system interfaced with computer for data acquisition (Fig. S2). The SS sensing chamber (volume ~1 l) has ports for injecting a known volume of target gas and a temperature controlled heating stage for adjusting the operating temperature of the sensors from RT to 300 °C. The gas sensor response (S) for NO₂ was calculated as R_a/R_g , where R_a and R_g were the sensor resistance in air and in test gas, respectively [10].

3 Results and discussion

3.1 Structural and optical characteristics

Figure 1 depicts XRD diffractograms obtained for both as-prepared and calcined samples. The XRD pattern of as-prepared samples is characterized by six dominant diffraction

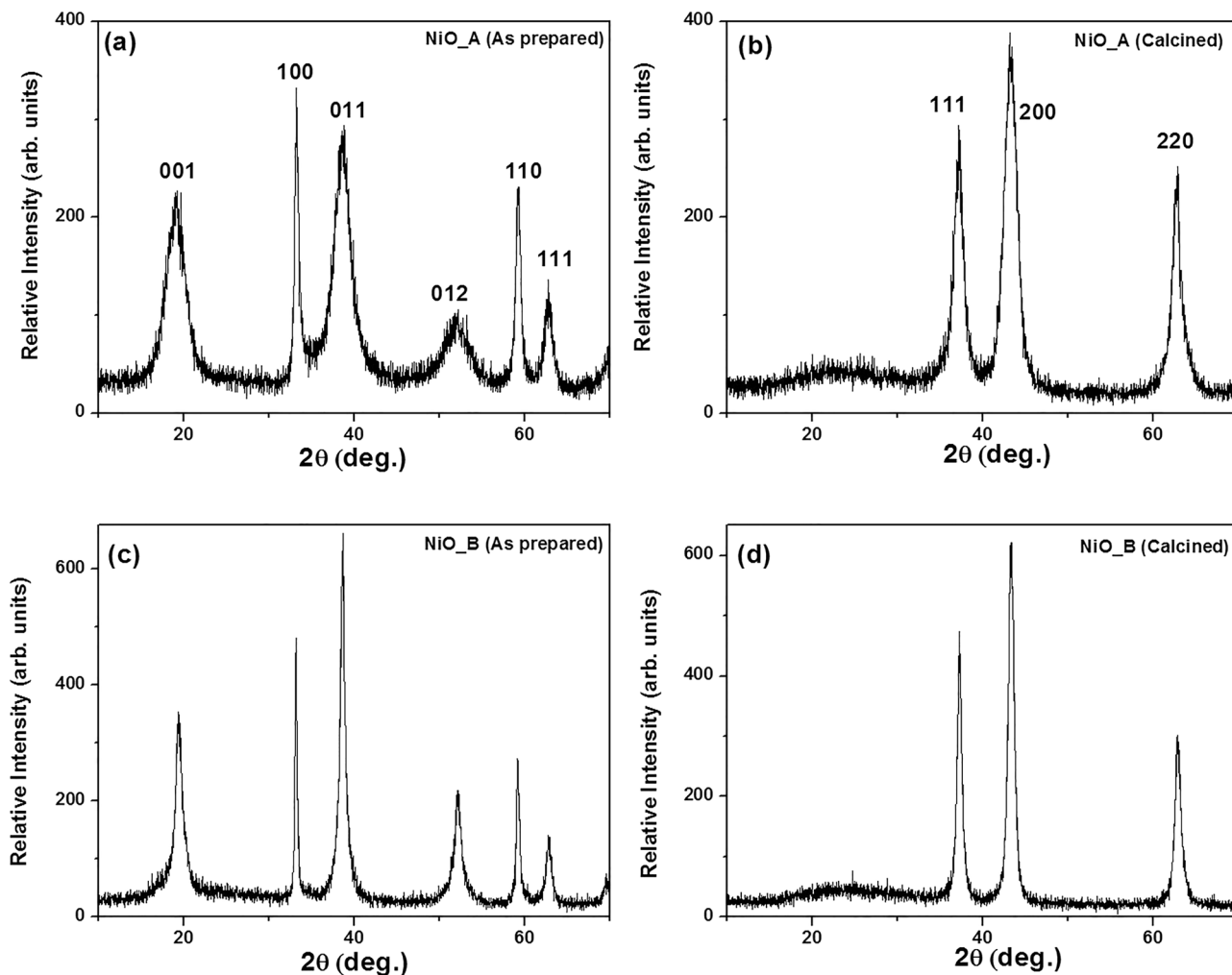


Fig. 1 XRD patterns of as-prepared and calcined NiO_A (a and b) and NiO_B (c and d)

peaks corresponding to (001), (100), (011), (012), (110) and (111) crystalline planes of hexagonal phase Ni(OH)₂ (JCPDS No. 73-1520). The calcined samples are featured by well-defined crystalline planes (111), (200) and (220), corresponding to the cubic phase of pure NiO (JCPDS No. 04-0835). Both co-precipitation (NiO_A) and thermochemically (NiO_B) synthesized samples showed similar XRD patterns though NiO_B showed higher diffraction peak intensities. The absence of additional peaks related to impurity/defects ascertains high purity of the prepared samples. The average crystallite size of the NiO nanoparticles is determined using Scherrer's formula:

$$D = \frac{0.9\lambda}{\beta \cos\theta},$$

where λ is the X-ray wavelength and β and θ represent the full width at half maximum (FWHM) and diffraction angle of the peaks. Considering instrumental broadening, the particle sizes of NiO samples prepared by co-precipitation and thermochemical methods are estimated as ~7 and 10 nm, respectively.

FESEM images of spray-coated NiO_A and NiO_B films on glass substrates are shown in Fig. 2. It is seen that both the samples are homogeneous and porous with randomly

distributed cauliflower like structures. Particles in NiO_B seem to be more agglomerated, which may reduce the effective surface area. Nevertheless, it is obvious that the particles are in the nanometer regime for both the films as confirmed by XRD. The EDAX spectrum of both the films yielded similar patterns (Fig. 2c). It is observed that the oxygen content showed higher contribution in both the films.

Figure 3 shows the transmittance and Tauc plots of the films. Both NiO_A and NiO_B films exhibit > 70% transmittance in the visible region. The optical band gap for both is calculated from Tauc's plot (Fig. 3b) using the relation [19]:

$$(\alpha h\nu)^2 = A(h\nu - E_g), \quad (1)$$

where α , $h\nu$, A and E_g are absorption coefficient, photon energy, dimensional constant and optical band gap, respectively. The estimated values of E_g are 3.59 and 3.39 eV for NiO_A and NiO_B, respectively, which are in accordance with the typical band gap value of NiO [19]. Slightly lower value of E_g for NiO_B could be attributed to the larger grain size than that of NiO_A.

In metal oxides, the photoluminescence emission is strongly influenced by various defect states such as metal deficiency and oxygen vacancy. If the material is relatively

Fig. 2 FESEM images of **a** NiO_A and **b** NiO_B. **c** Representative EDX spectrum of NiO

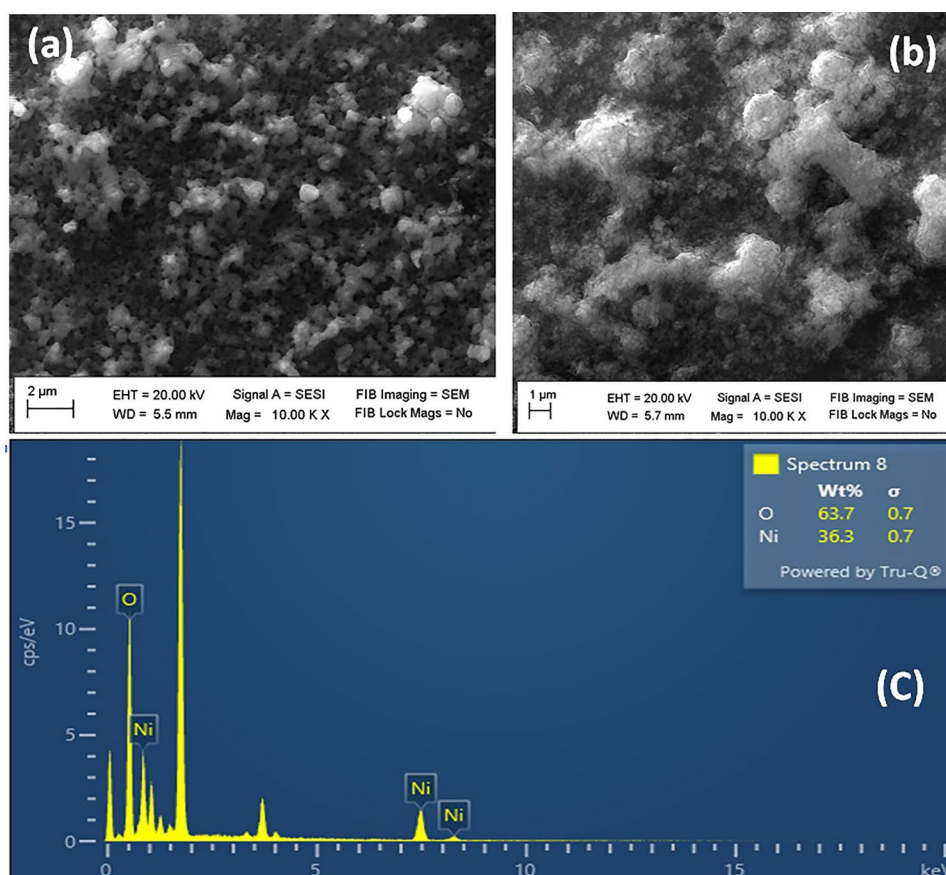


Fig. 3 a Transmittance and b Tauc plots of NiO_A and NiO_B

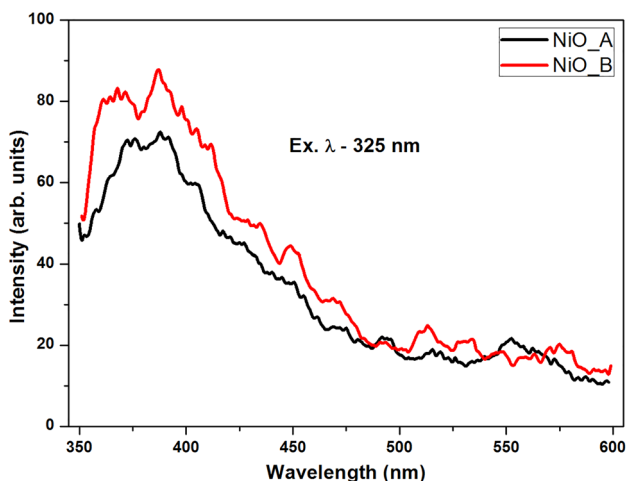
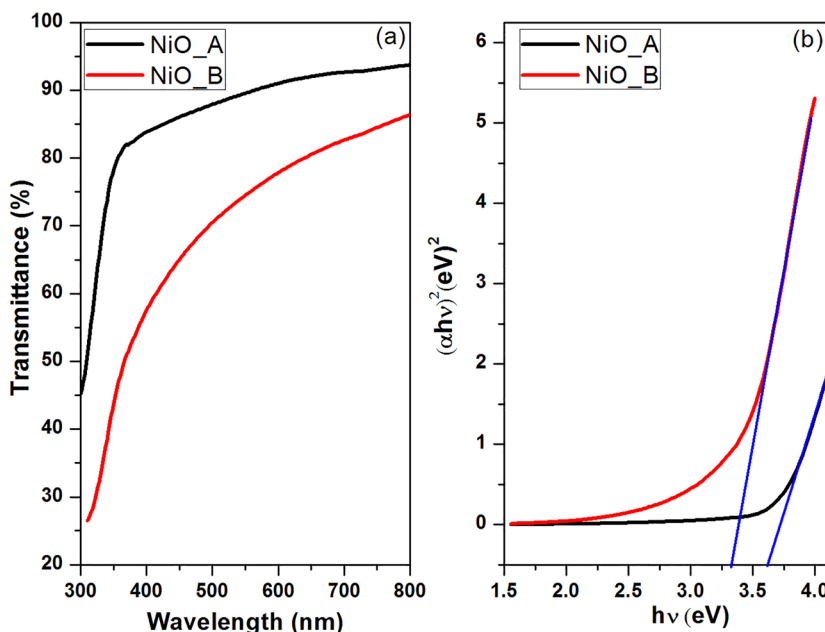


Fig. 4 Room-temperature photoluminescence spectra of NiO_A and NiO_B

free of defects, only a strong near band edge (NBE) emission will be seen. Figure 4 shows the room-temperature PL spectra of NiO_A and NiO_B under an excitation wavelength of 325 nm. Both the films feature two overlapping peaks in the UV region around 368 and 390 nm. These peaks represent the NBE emissions resulting from the $3d^8-3d^8$ transition of Ni²⁺ ions as reported by many researchers [20, 21]. Emission bands in the visible region (> 400 nm) are generally associated with various defect states and/or impurities. Accordingly, the broad emission tail extending from 420 to 580 nm could be attributed to the radiative transitions from Ni interstitial (Ni_i), doubly

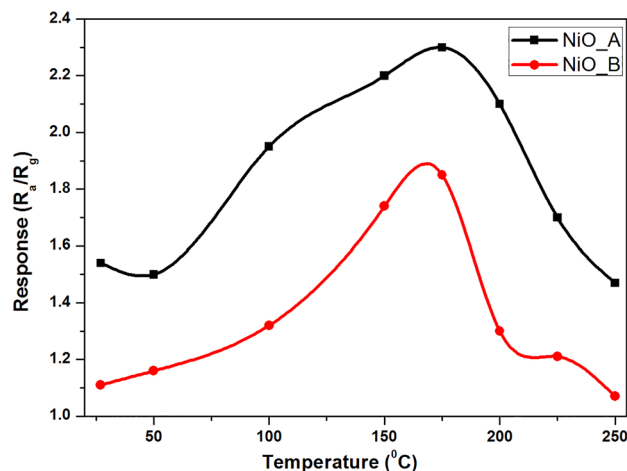


Fig. 5 Response of NiO_A and NiO_B sensors as a function of temperature for 5 ppm NO₂

ionized Ni vacancy (V_{Ni}²⁻), nickel and oxygen vacancies [22, 23].

3.2 Gas sensing studies

The spray-coated NiO sensors are subjected to the evaluation of 4 s parameters (sensitivity, speed, selectivity and stability) which determine the figure of merit for any gas sensor. As these parameters are temperature dependent, it is crucial to find the optimum operating temperature. Figure 5 shows the response of both the sensors for an exposure of 5 ppm NO₂ as a function of sensor temperature. It is evident that both the sensors show optimum

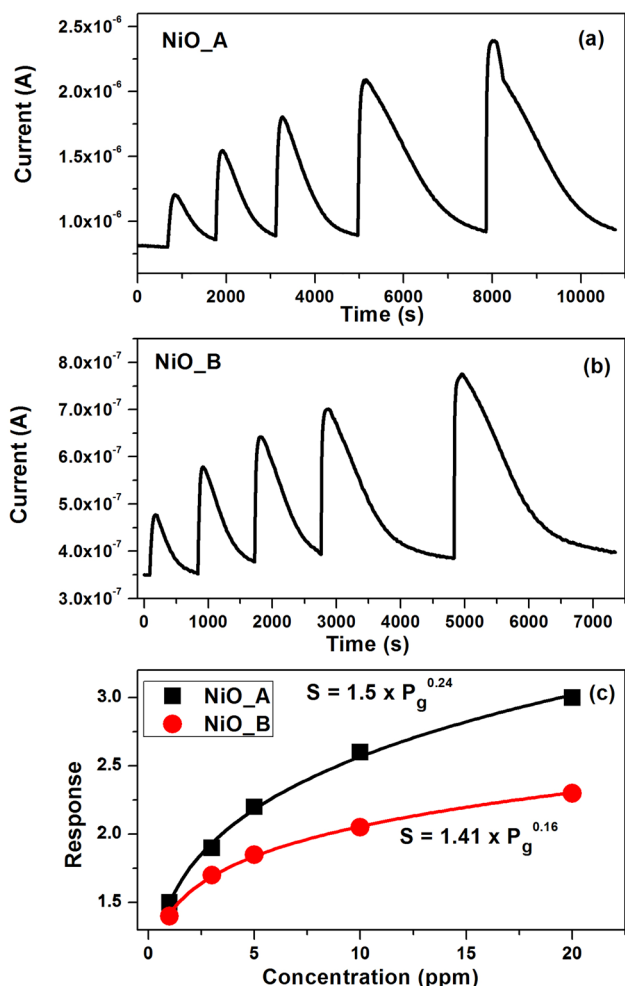


Fig. 6 Response and recovery characteristics of **a** NiO_A and **b** NiO_B at 180 °C as a function of NO₂ concentration; **c** comparison of sensor response with NO₂ concentration at 180 °C

response for an operating temperature of ~ 180 °C. Below and above 180 °C, the response tends to deteriorate; hence, detailed studies are carried out at an operating temperature of 180 °C.

The dynamic response and recovery characteristics of both sensors for different concentration of NO₂ at 180 °C are depicted in Fig. 6a and b. Both sensors exhibit fast response upon gas exposure and recover back to the base current, when exposed to air. For 5 ppm concentration, the response (*t*₉₀) times are 70 and 50 s for NiO_A and NiO_B, respectively. Similarly, the recovery times (*t*₁₀) are estimated as ~ 15 and 11 min for NiO_A and NiO_B, respectively. Figure 6(c) shows the comparison of response as a function of NO₂ concentration. The response of chemiresistive MOX gas sensor generally follows power law as given by [24]:

$$S = cP_g^\alpha$$

where *P_g* is the gas concentration and *c* and *α* are constants, which depend on the physico-chemical properties of sensor material and reaction with the target gas. It is seen from Fig. 6c that the response of both the sensors obeys the power law. Nevertheless, it is clear that the response of NiO_A is superior though NiO_B has slightly faster dynamics.

Repeatability and reversibility tests of the sensors are carried out for four sensing cycles of 5 ppm of NO₂ at 180 °C (Fig. 7). The variation in response between each cycle is found to be < 10%, and after each cycle, the sensor current reversed back to the base line.

Selectivity is an important parameter which enables the sensor to distinguish the target gas in the presence of other intrusive gases as in the case of real time applications. Figure 8 illustrates the response of NiO_A and NiO_B for 5 ppm of various gases at 180 °C. It is seen that both the sensors are highly selective to only NO₂. Stability of the

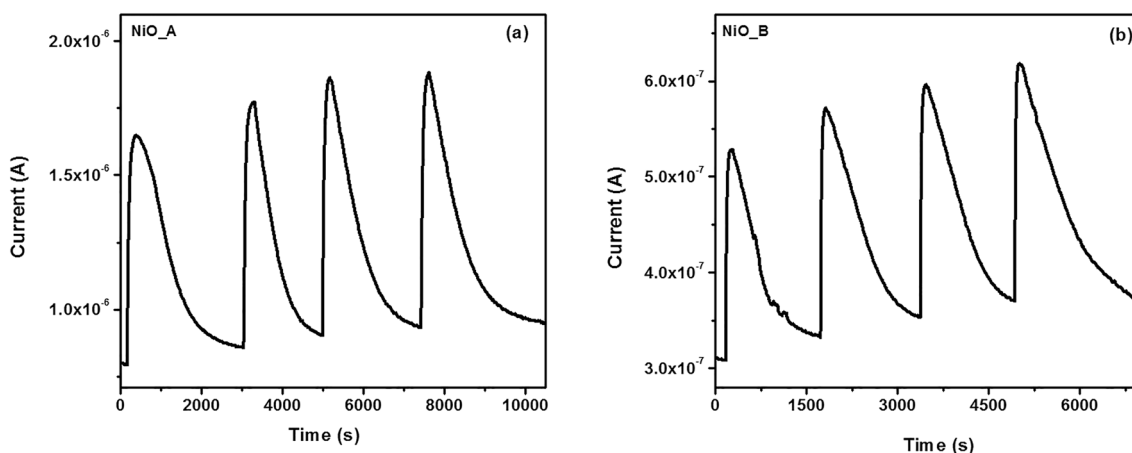


Fig. 7 Repeatability and reversibility of **a** NiO_A and **b** NiO_B for 5 ppm of NO₂ at 180 °C

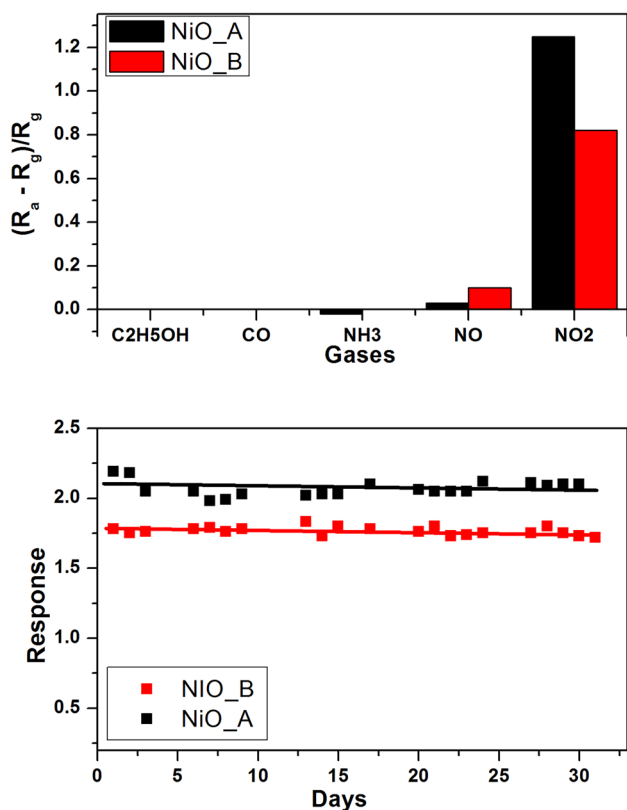


Fig. 8 Response of NiO sensors at 180 °C for 5 ppm of **a** various gases and **b** NO₂ for a period of one month

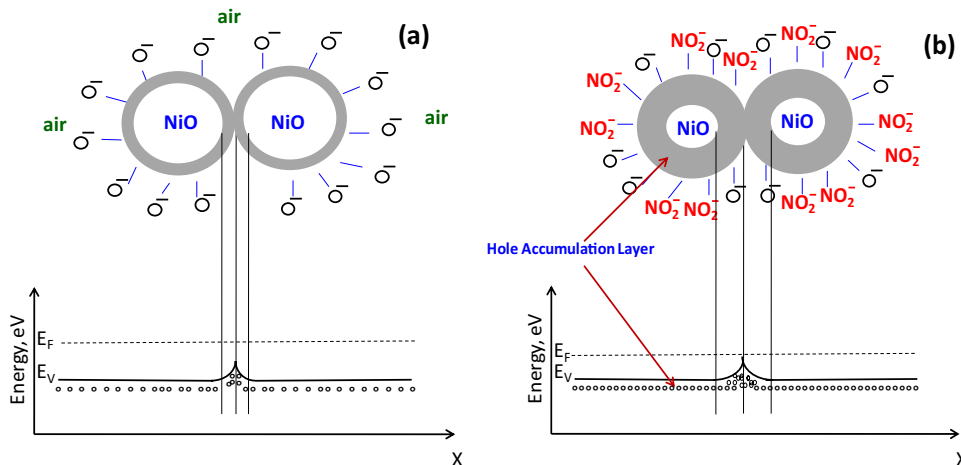
sensing response validates the feasibility for long-term use of the sensors in real-time applications.

Figure 8b shows the sensor response measured over a period of one month for 5 ppm of NO₂ at 180 °C. It is seen that the response is very stable, substantiating the good long-term stability of the sensors.

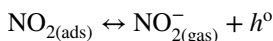
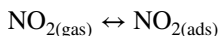
3.3 NO₂ sensing mechanism

It is widely reported that the n-type or the p-type semiconductor in metal oxides arises due to abundance or deficiency of metal ions in the material. Accordingly, when oxygen anions adsorb, an electron depletion layer (EDL) is formed near the surface of n-type MOX, whereas a hole accumulation layer (HAL) is formed in case of p-type semiconductor [10]. The extent of charge carriers depends on various conditions such as synthesis method, morphology, dopant concentration and operating temperature. In addition to ionization as holes, the metal cation defects in p-type MOX act as favourable adsorption sites depending on the gas and the MOX material. However, it has been reported that adsorption of oxidizing gases is not favoured generally by p-type MOX materials as the analyte gas has to extract electrons from the valence band [23]. Nonetheless, non-stoichiometry plays an important role in MOX sensors; specifically in case of NiO, abundance of vacancies at Ni²⁺ sites enhances the adsorption as well as sensitivity towards NO₂ [26]. These nickel vacancies form a shallow acceptor level above the valence band of NiO [27]. Based on our experimental results, the probable sensing mechanism for NO₂ is pictorially depicted in Fig. 9. When the NiO sensor is exposed to ambient air, the adsorption of oxygen anions attracts few electrons from the valence band and create a hole accumulation layer near the surface of NiO nanoparticles (Fig. 9a). The surface conductivity depends on the hole concentration, which in our case is found to be more in co-precipitated NiO nanoparticles. When the sensor is exposed to NO₂, the analyte gas molecules are physisorbed on the surface and extract electrons from the acceptor level created by nickel vacancies (Fig. 9b). The adsorption of NO₂ is dominant due to its higher electron affinity (~2.28 eV) compared to that of oxygen (~0.43 eV) [28]. Accordingly, the adsorbed molecules oxidize the Ni²⁺ to Ni³⁺ and expand the HAL by releasing holes, thereby increasing the surface

Fig. 9 Schematic diagram and energy band model for NO₂ sensing mechanism when exposed to **a** air and **b** NO₂



conductivity [29]. The adsorption of NO₂ and the release of holes are governed by the following reactions [28]:



Using DFT calculations, Wang et al. have computed the adsorption energies of NO₂, H₂S, and NH₃ molecules on NiO (100) surface and found the interaction of NO₂ molecule was stronger with NiO surface [30]. Zhang et al. [26] have demonstrated by in situ DRIFT studies that the abundance of nickel vacancies led to greater sensitivity for NO₂ in mesoporous NiO nanosheets. They concluded that the strong interaction of doubly charged nickel vacancies with NO₂ further facilitated the ionization of neutral nickel vacancies, thus providing more adsorption sites for NO₂. Additionally, Ni has superior catalytic properties which can also greatly aid NO_x reduction on NiO surface, resulting in enhanced gas sensitivity [31]. In the present study, the broad emission in the visible region of photoluminescence spectra of both NiO_A and NiO_B confirms the presence of various defects and vacancies. For the same sensor configuration, the surface conductivity of NiO_A is found to be higher which is mainly determined by the extent of nickel vacancies. Hence, the superior sensitivity of NiO_A could be attributed to substantial amount of nickel vacancies as compared to NiO_B. For nanoparticles synthesized by co-precipitation method (NiO_A), the precipitation process occurs at much faster rate, as compared to that of thermochemical method (NiO_B). As slower precipitation rate affords higher crystallinity, NiO_B displays higher crystallinity as evident from the XRD patterns (Fig. 1). Besides, the lattice parameters calculated for both the samples showed a deviation of 0.4% (NiO_A, 4.185 Å) and 0.27% (NiO_B, 4.179 Å) from the ideal crystal lattice parameter of NiO (4.168 Å). This deviation could be attributed to existence of crystal defects and the non-stoichiometric composition of the sample, which is higher for NiO_A [32]. The resultant smaller size grains of NiO_A can provide more adsorption sites, higher surface energy and fast diffusion rates, leading to enhanced sensitivity for NO₂.

4 Conclusions

Facile synthesis of NiO nanoparticles was carried out by co-precipitation (NiO_A) and thermochemical (NiO_B) methods. Structural, morphological and optical characterizations confirmed the formation of nanocrystalline NiO particles with non-stoichiometric defects and vacancies. Gas sensing measurements corroborated the high sensitivity, selectivity

and reversibility of both NiO_A and NiO_B nanoparticles for NO₂ at a moderate operating temperature of 180 °C. Probable sensing mechanism for NO₂ was proposed based on the photoluminescence studies, which confirmed substantial amount of nickel vacancies. Further, the smaller size grains of co-precipitated NiO nanoparticles resulted in better NO₂ gas sensitivity.

Supplementary Information The online version contains supplementary material available at <https://doi.org/10.1007/s00339-022-05766-9>.

Declarations

Conflict of interest The authors declare that they have no known competing interests or personal relationships that could have appeared to influence the work reported in this paper. We further declare that no grants from any funding agencies were received for carrying out this research work.

References

1. X. Liu, S. Cheng, H. Liu, S. Hu, D. Zhang, H. Ning, *Sensors* **12**, 9635 (2012)
2. J.M. Walker, S.A. Akbar, P.A. Morris, *Sens. Actuators B Chem.* **286**, 624 (2019)
3. G. Eranna, B.C. Joshi, D.P. Runthala, R.P. Gupta, *Crit. Rev. Solid State Mater. Sci.* **29**, 111 (2004)
4. T.P. Mokoena, H.C. Swart, D.E. Motaung, *J. Alloy. Compd.* **805**, 267 (2019)
5. P. Gupta, K. Kumar, N.K. Pandey, B.C. Yadav, S.H. Saeed, *Appl. Phys. A* **127**, 289 (2021)
6. S.-H. Kwon, T.-H. Kim, S.-M. Kim, S. Oh, K.-K. Kim, *Nanoscale* **13**, 12177 (2021)
7. K.G. Girija, K. Somasundaram, A.K. Debnath, A. Topkar, R.K. Vatsa, *J. Mater. Chem. Phys.* **214**, 297 (2018)
8. N. Han, H. Liu, X. Wu, D. Li, L. Chai, Y. Chen, *Appl. Phys A* **104**, 627 (2011)
9. X.-T. Yin, J. Li, Q. Wang, D. Dastan, Z.-C. Shi, N. Alharbi, H. Garmestani, X.-M. Tan, Y. Liu, X.-G. Ma, *Langmuir* **37**, 13548 (2021)
10. H.-J. Kim, J.-H. Lee, *Sens. Actuators B Chem.* **192**, 607 (2014)
11. Y. Gong, S. Zhang, H. Gao, Z. Ma, S. Hu, Z. Tan, *Sustain Energy Fuels* **4**, 4415 (2020)
12. M. Kandasamy, A. Seetharaman, D. Sivasubramanian, A. Nithya, K. Jothivenkatachalam, N. Maheswari, M. Gopalan, S. Dillibabu, A. Eftekhari, *ACS Appl. Nano. Mater.* **1**, 5823 (2018)
13. S.J. Mezher, M.O. Dawood, A.A. Beddai, M.K. Mejbel, *Mater. Technol.* **35**, 60 (2020)
14. I. Fasaki, A. Koutoulaki, M. Kompitsas, C. Charitidis, *Appl. Surf. Sci.* **257**, 429 (2010)
15. G. Korotcenkov, *Nanomaterials* **10**, 1392 (2020)
16. H.T. Rahal, R. Awad, A.M. Abdel-Gaber, D. El-Said Bakeer, *J. Nanomater.* **2017**, 1–9 (2017). <https://doi.org/10.1155/2017/7460323>
17. M. Mohammadijoo, Z.N. Khorshidi, S.K. Sadrnezhaad, V. Mazinani, *Nanosci. Nanotechnol. Int. J.* **4**, 6 (2014)
18. X. Deng, Z. Chen, *Mater. Lett.* **58**, 276 (2004)
19. M.M. Gomaa, M.H. Sayed, V.L. Patil, M. Boshta, P.S. Patil, *J. Alloy. Compd.* **885**, 160908 (2021)
20. B. Karthikeyan, T. Pandiyarajan, S. Hariharan, M.S. Ollakkan, *CrystEngComm* **18**, 601 (2016)

21. D. Adler, J. Feinleib, *Phys. Rev. B* **2**, 3112 (1970)
22. A.C. Gandhi, S.Y. Wu, *Nanomaterials* **7**, 231 (2017)
23. A.A. Ezhilarasi, J.J. Vijaya, K. Kaviyarasu, M. Maaza, A. Ayeshamariam, L.J. Kennedy, *J. Photochem. Photobiol. B Biol.* **164**, 352 (2016)
24. S. Zhao, Y. Shen, P. Zhou, J. Zhang, W. Zhang, X. Chen, D. Wei, P. Fang, Y. Shen, *Ceram. Int.* **44**, 753 (2018)
25. J. Zhang, D. Zeng, Q. Zhu, J. Wu, Q. Huang, C. Xie, *J. Phys. Chem. C* **120**, 3936 (2016)
26. X. Geng, D. Lahem, C. Zhang, C.-J. Li, M.-G. Olivier, M. Debliquy, *Ceram. Int.* **45**, 4253 (2019)
27. M. Arif, A. Sanger, A. Singh, *J. Electron. Mater.* **47**, 3451 (2018)
28. N.D. Hoa, S.A. El-Safty, *Chem. Eur. J.* **17**, 12896 (2011)
29. M. Wang, Y. Wang, J. Liu, C. Pei, B. Liu, Y. Yuan, H. Zhao, S. Liu, H. Yang, *Sens. Actuators B Chem.* **250**, 208 (2017)
30. B. Wang, J. Nisar, R. Ahuja, *A.C.S. Appl. Mater. Interfaces* **4**, 5691 (2012)
31. S. Das, K.G. Girija, A.K. Debnath, R.K. Vatsa, *J. Alloys Compd.* **854**, 157276 (2021)
32. S.M. Meybodi, S.A. Hosseini, M. Rezaee, S.K. Sadrnezhad, D. Mohammadyani, *Ultrason. Sonochem.* **19**, 841 (2012)

Publisher's Note Springer Nature remains neutral with regard to jurisdictional claims in published maps and institutional affiliations.